ARTICLE

Modulating the Coordination Environment of Atomically Dispersed Nickel for Efficient Electrocatalytic CO_2 Reduction at Low Overpotentials and Industrial Current Densities

Yichen Sun, Xiaolu Liu, Jiazheng Tian, Zixuan Zhang, Yang Li, Yinghui Xie, Mengjie Hao, Zhongshan Chen, Hui Yang,* Geoffrey I. N. Waterhouse, Shengqian Ma,* and Xiangke Wang*

Read Online

ACCESS | Metrics & More | Article Recommendations | SI Supporting Information

ABSTRACT: Electrocatalytic CO_2-to-CO conversion with a high CO Faradaic efficiency (FE_{CO}) at low overpotentials and industrial-level current densities is highly desirable but a huge challenge over non-noble metal catalysts. Herein, graphitic N-rich porous carbons supporting atomically dispersed nickel (NiN_4−O sites with an axial oxygen) were synthesized (denoted as O−Ni−N_x−GC) and applied as the cathode catalyst in a CO_2RR flow cell. O−Ni−N_x−GC showed excellent selectivity with a FE_{CO} over 92% at low overpotentials ranging from 17 to 60 mV, and over 99% at 80 mV. The FE_{CO} was ~100% at industrial-level current densities from 200 to 900 mA·cm^{-2}. Impressively, O−Ni−N_x−GC delivered a state-of-the-art FE_{CO} of >96% at 1 A·cm^{-2} with a turnover frequency of 81.5 s^{-1} in a 1 M KOH electrolyte. O−Ni−N_x−GC offered excellent stability during long-term operation for 140 h at 100 mA·cm^{-2}, maintaining a FE_{CO} > 99%. Mechanism studies revealed that the axial oxygen at the atomically dispersed nickel sites enhanced electron delocalization, with the graphitic N-rich porous carbon support lowering the CO_2-to-CO energy barrier and inducing a negative shift in the Ni-3d d-band center, effectively promoting the formation of the *COOH intermediate while weakening the adsorption of the *CO intermediate, thus optimizing the catalytic activity/selectivity to CO under practical conditions.

KEYWORDS: metal−nitrogen−carbon, NiN_4-O site, CO_2 electroreduction, high FE_{CO}, ampere-level current density
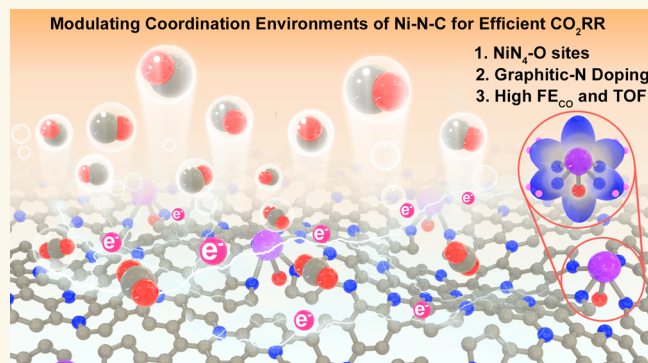
The electrocatalytic carbon dioxide reduction reaction (CO_2RR) offers a promising strategy for achieving global carbon balance and avoiding the worst impacts of climate change caused by anthropogenic CO_2 emissions.[1−4] Utilizing renewably generated electricity in combination with efficient electrocatalysts to convert CO_2 into high-value bulk chemicals and carbon-neutral fuels, CO_2RR emerges as a vital process in the pathway to decarbonization.[5,6] Among the various possible products of electrocatalytic CO_2 reduction, CO holds significant importance as a feed in many important industrial chemical processes, especially Fischer−Tropsch syntheses of multicarbon oxygenates and hydrocarbon products.[7] Further, CO is used as a reducing agent in the manufacture of steel. For electrocatalytic CO_2-to-CO conversions at industrial-scale, it is essential to develop catalysts

that exhibit high activity, high selectivity to CO, a high turnover frequency (TOF), high energy conversion efficiency, and excellent durability under ampere-level current densities.[8−11] However, finding catalysts that satisfy all of the aforementioned criteria has proved a huge challenge to date, especially catalysts that can achieve nearly 100% Faradaic efficiency to CO (FE_{CO}) at high current densities (>200 mA·
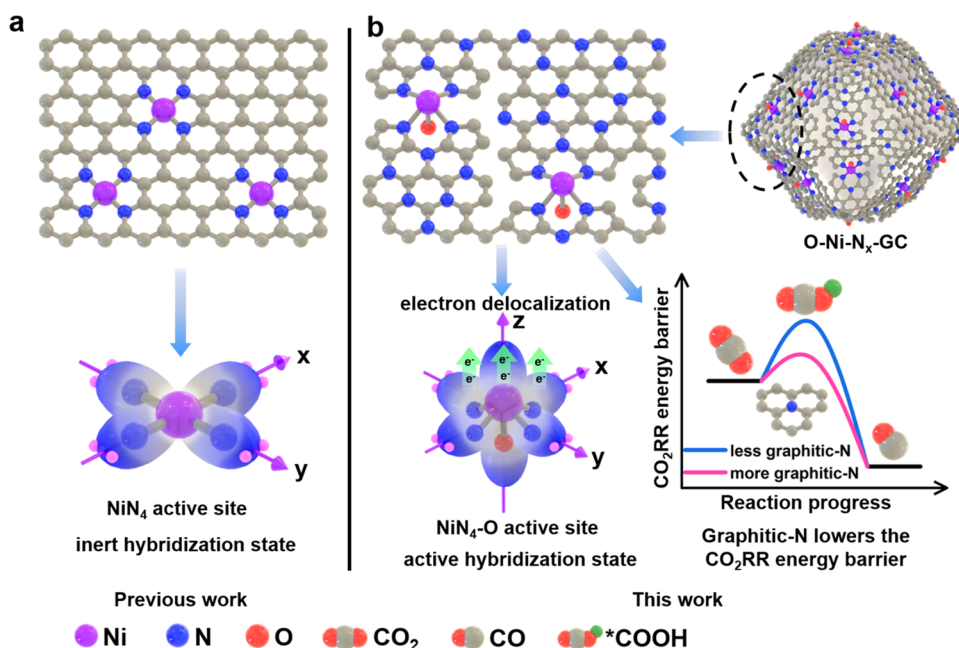
Figure 1. The general strategy for electrocatalytic CO_2 reduction in our study. (a) Schematic illustration of the carbon supported NiN_4 catalyst. (b) Schematic illustration of the synthesized graphitic N-doped porous carbon supported NiN_4—O active sites (denoted as O—Ni—N_x—GC). Highlight the graphitic-N and NiN_4—O sites to lower the CO_2RR energy barrier.

cm^{-2}) without the occurrence of the competing hydrogen evolution reaction (HER).[12−15] This work represents a significant advancement by addressing these challenges through the rational design of a novel NiN_4—O coordinated catalyst that delivers outstanding performance under industrial conditions with almost no occurrence of HER.

Recently, metal−nitrogen-carbon (M−N−C) catalysts have emerged at the forefront of electrocatalytic CO_2RR due to their low-cost, near maximal metal atom utilization, well-defined active sites, and excellent chemical/electrochemical stability.[16−21] Most reported M−N−C typically exhibit a planar phthalocyanine-like structures (MN_4), where the square-planar MN_4 moieties are considered the primary active sites. However, certain MN_4 species, owing to their higher structural/electronic symmetry, exhibit chemical inertness, hampering electron transfer to reactants to some extent.[22,23] Particularly, the electrocatalytic CO_2-to-CO conversion performance of most M−N−C catalysts is limited under industrial current density conditions due to significant increases in overpotential, and their stability is also adversely impacted under such high current densities, reducing the energy conversion efficiency.[24,25] A recent notable contribution reported a method utilizing single-atom nickel-decorated carbon membranes for CO_2 electroreduction, achieving stable performance over a 120 h testing period at a current density of 308.4 mA·cm^{-2} with FE_{CO} > 95%.[26] Although this work signifies a significant advancement in the field, it should be noted that the FE_{CO} obtained at low overpotentials was relatively low, with the maximum CO partial current density (j_{CO}) reaching only 336.5 mA·cm^{-2} with a FE_{CO} of 83%. These results indicate there is still substantial scope for improvement in the design of M−N−C electrocatalysts to meet the practical requirements of electrocatalytic CO_2-to-CO conversion with high FE_{CO} under both low overpotential and high current density conditions.

To simultaneously achieve efficient electrocatalytic CO_2-to-CO conversion performance at both low overpotentials and high current densities, we herein designed and synthesized graphitic N-rich porous carbon hollow capsules supporting atomically dispersed nickel. The nickel sites possessed a NiN_4—O coordination, consisting of a square-planar NiN_4 with an axial oxygen, with the developed O−Ni−N_x−GC catalyst outperforming traditional M−N−C catalysts for CO_2RR to CO (Figure 1). The introduction of axial oxygen (NiN_4−O) enhances the electron delocalization at the nickel center, which together with graphitic N-rich porous carbon support lowers the energy barrier for the formation of the *COOH intermediate and the desorption of the *CO intermediate, enabling O−Ni−N_x−GC to deliver excellent catalytic performance over a wide current density range from 10 mA·cm^{-2} to 1 A·cm^{-2} (corresponding overpotentials ranged from 17.4 mV to 2 V, vs RHE, with iR correction) in a 1 M KOH electrolyte. Through detailed experimental studies, O−Ni−N_x−GC achieved a record high TOF of 81.5 s^{-1} with ~100% Faradaic efficiency for FE_{CO} across a broad current density range from 100 to 900 mA·cm^{-2}, far exceeding reported M−N−C catalysts and other state-of-the-art catalysts under similar conditions. Moreover, O−Ni−N_x−GC demonstrates exceptional stability, maintaining a FE_{CO} > 99% over 140 h at a current density of 100 mA·cm^{-2} in a 1 M KOH electrolyte. The excellent performance of the developed O−Ni−N_x−GC catalyst and the cooperative functions of specific components guide the rational design of efficient electrocatalyst for CO_2-to-CO conversion under industrial conditions.

RESULTS AND DISCUSSION

Synthesis and Characterization of Materials. To address the challenge of efficient electrocatalytic CO_2-to-CO conversion at both low overpotentials and industrially relevant current densities, graphitic N-rich porous carbon capsules functionalized with atomically dispersed nickel with a NiN_4−O
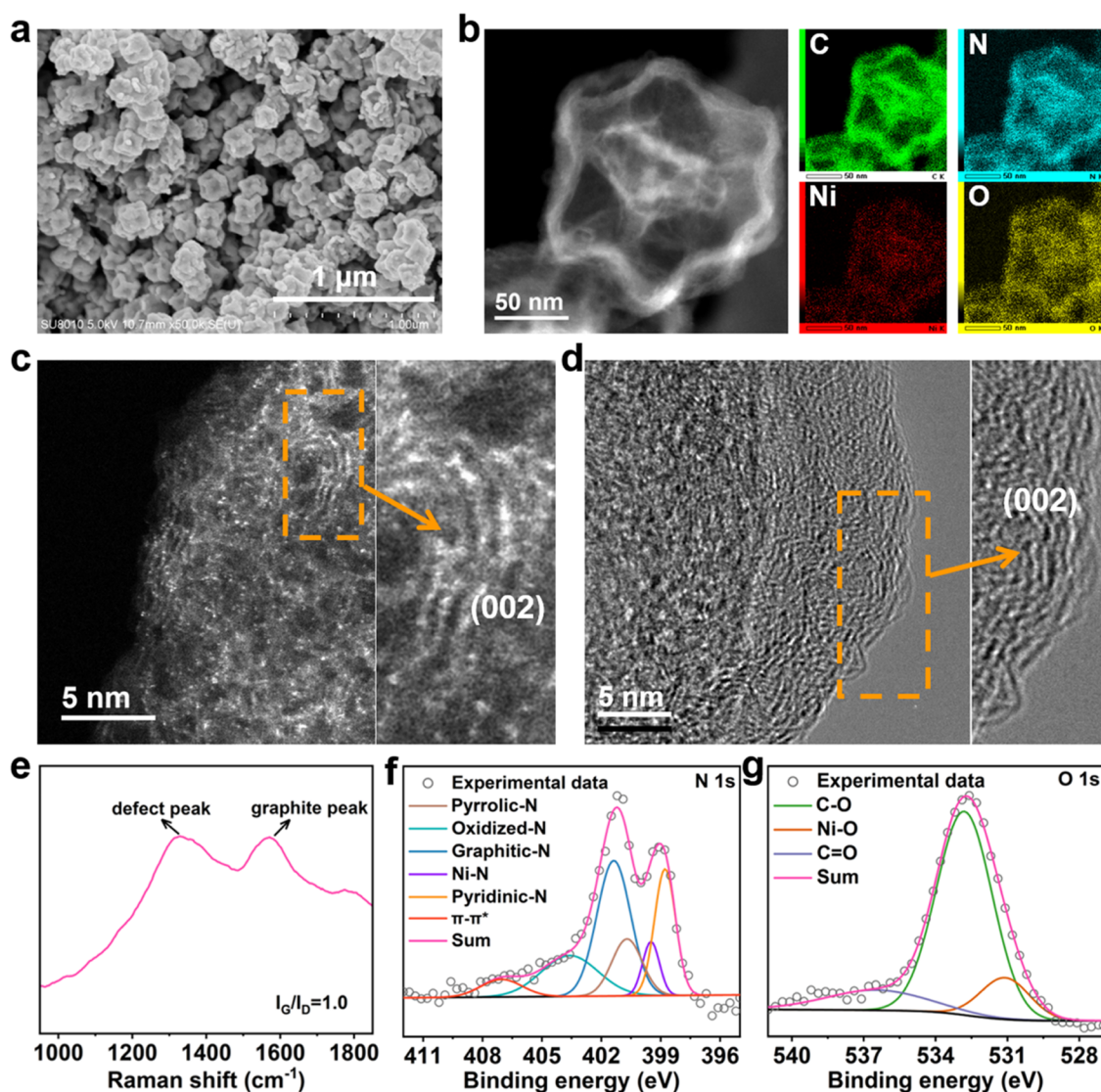
Figure 2. Structural characterization of O−Ni−N$_x$−GC. (a) SEM image of O−Ni−N$_x$−GC. (b) HAADF-STEM and corresponding EDS mapping images for O−Ni−N$_x$−GC. (c, d) Spherical-aberration-corrected HAADF-STEM and TEM images for O−Ni−N$_x$−GC (highlighting the atomically dispersed Ni sties and graphitic-N doped carbon). (e) Raman spectrum for O−Ni−N$_x$−GC. f, g N 1s and O 1s X-ray photoelectron spectra (XPS) for O−Ni−N$_x$−GC.

coordination (O−Ni−N$_x$−GC) were synthesized (Figure S1). Initially, ZIF-8 nanocrystals were synthesized and then coated with a potassium-tannic acid (TA) coordination polymer, yielding a ZIF-8@K-TA (Figures S2 and S3). Subsequently, potassium cations were replaced by nickel ions though ion-exchange in a Ni(NO$_3$)$_2$·6H$_2$O/methanol solution, producing ZIF-8@Ni-TA. Next, the ZIF-8@Ni-TA was pyrolyzed at 1000 °C in an argon atmosphere, followed by etching with hydrochloric acid (HCl) and a second pyrolysis at 1000 °C, resulting in atomically dispersed NiN$_4$−O immobilized on graphitic nitrogen-rich porous carbon capsules. Scanning electron microscopy (SEM) revealed that O−Ni−N$_x$−GC possessed polyhedral morphology, similar to the ZIF-8, ZIF-8@K-TA, and ZIF-8@Ni-TA (Figures 2a and S4). Low-magnification high-angle annular dark field scanning transmission electron microscopy (HAADF-STEM) images showed the hollow morphology, and corresponding energy-dispersive X-ray spectroscopy (EDS) images revealed uniform distribution of C, N, Ni, and O through the O−Ni−N$_x$−GC sample (Figure 2b). Spherical-aberration-corrected HAADF-STEM

further revealed the presence of highly dispersed bright spots (average size ∼0.2 nm), verifying the existence of atomically dispersed Ni species on the hollow capsules (Figure 2c). No large nanoparticles were observed, reaffirming the high dispersion of Ni in the sample. Notably, the O−Ni−N$_x$−GC catalyst exhibited a pronounced graphitic structure, evidenced by the typical (002) basal planes, indicating a high degree of graphitization (Figure 2c,d). This was further confirmed by Raman spectroscopy, where the I_G/I_D intensity ratio was ∼1.0 (Figure 2e).[27,28] Powder X-ray diffraction (PXRD) showed two distinct peaks at ∼25 and ∼44°, attributed to the (002) and (101) planes of graphite (PDF#75-1621-Graphite, Figure S5).[29,30] No peaks associated with Ni metal or Ni oxides were seen. The elemental composition of O−Ni−N$_x$−GC was probed using inductively coupled plasma mass spectrometry (ICP-MS) and elemental analysis (EA), with the nickel and nitrogen contents determined to be 1.04 and 5.6 wt %, respectively (Table S1).

X-ray photoelectron spectroscopy (XPS) and X-ray Absorption Spectroscopy (XAS) were next employed to
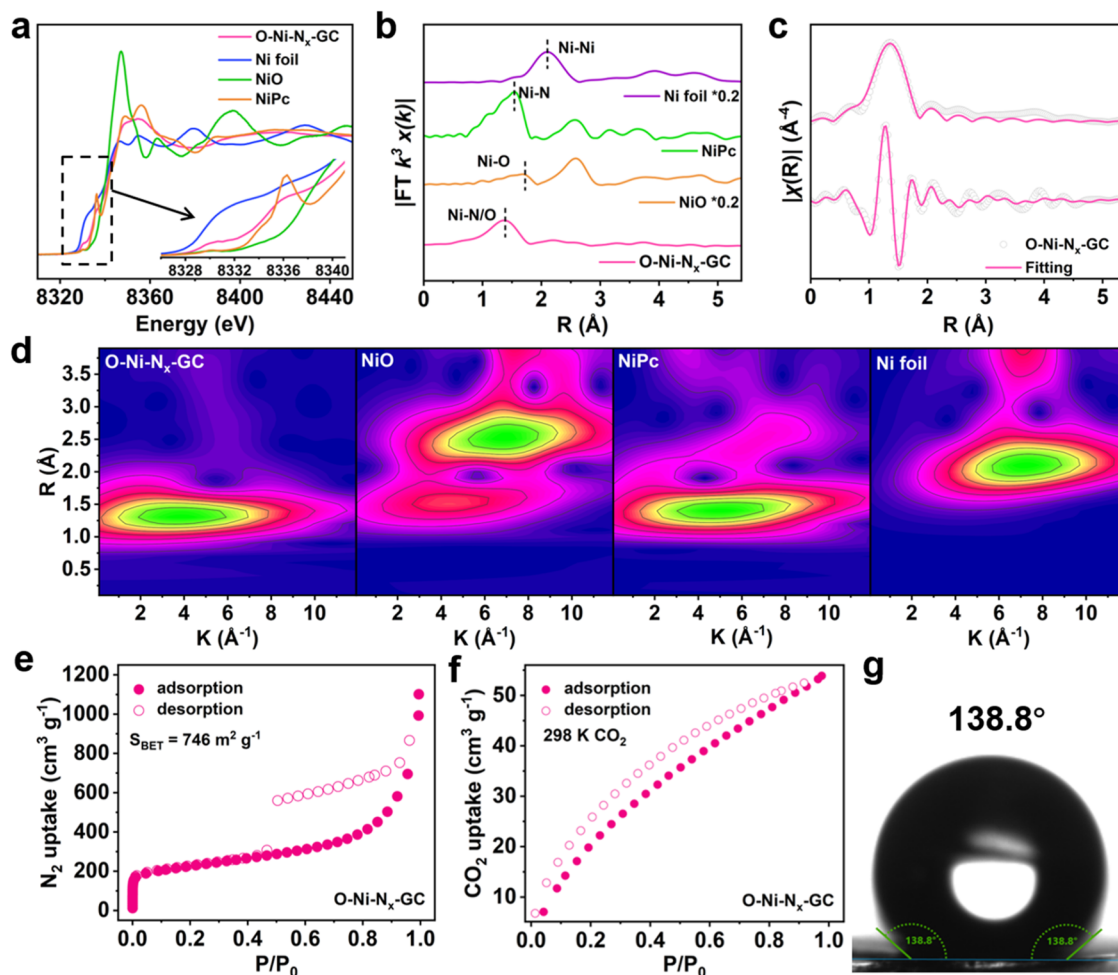
Figure 3. Electronic structure, Ni coordination geometry and water contact angle of O−Ni−N$_x$−GC. (a) Ni K-edge XANES spectra for O−Ni−N$_x$−GC, Ni foil, NiO, and NiPc. (b) Corresponding EXAFS spectra for O−Ni−N$_x$−GC, Ni foil, NiO, and NiPc. (c) EXAFS fitting of data for O−Ni−N$_x$−GC in R space. (d) WT contour plots for O−Ni−N$_x$−GC, Ni foil, NiO, and Nipc. (e) N$_2$ sorption isotherms for O−Ni−N$_x$−GC measured at 77 K. (f) CO$_2$ sorption isotherms for O−Ni−N$_x$−GC measured at 298 K. (g) Contact angle for a water droplet on pressed pellets of O−Ni−N$_x$−GC.

explore the electronic structure of O−Ni−N$_x$−GC. The XPS survey spectrum showed the presence of C, N, O, and Ni elements in O−Ni−N$_x$−GC (Figure S6). The high-resolution C 1s spectra showed C−C, C−N, and C−O/C=O peaks, confirming the successful doping of N and O in O−Ni−N$_x$−GC (Figure S6). The additional $\pi-\pi^*$ signal in the C 1s spectrum proved the high degree of graphitization in O−Ni−N$_x$−GC.[31] The high-resolution N 1s XPS spectrum showed peaks due to pyridinic-N (~398.7 eV), pyrrolic-N (~400.7 eV), graphitic-N (~401.3 eV), oxidized-N (~403.6 eV) and $\pi-\pi^*$ (~407.0 eV) in O−Ni−N$_x$−GC, with the graphitic-N content ~35.2% of total N (Figure 2f).[32−34] The additional peak at ~399.5 eV corresponds to pyrrolic-nitrogen species forming Ni−N$_x$ bonds through coordination with Ni atoms, suggesting that O−Ni−N$_x$−GC mainly contains pyrrolic-type Ni−N structures.[15] As shown in Figure 2g, the high-resolution O 1s XPS spectra of O−Ni−N$_x$−GC displayed a peak centered at 531.2 eV, which can be attributed to the formation of the Ni−O bond.[35] The Ni 2p spectrum showed peaks at ~855 eV (Ni 2p$_{3/2}$) and 872.3 eV (Ni 2p$_{1/2}$) in a 2:1 area ratio, indicating O−Ni−N$_x$−GC contained Ni^{2+} ions (Figure S6).[36] The observation of Ni^{2+} "shake-up" satellites in the XPS spectrum verified this hypothesis.

XAS measurements were carried out to further elucidate the Ni oxidation state and local coordination geometry of Ni atoms in O−Ni−N$_x$−GC. NiO, nickel phthalocyanine (NiPc), and Ni foil were used as reference materials. The Ni K-edge X-ray absorption near edge structure (XANES) spectra reveal that the absorption edge of O−Ni−N$_x$−GC was similar to those of NiO and NiPc (Figure 3a), indicating that the oxidation state of nickel ions was likely +2, consistent with the XPS results.[25] The pre-edge features in the XANES spectra showed a peak ~8330 eV (representing a quadrupole-allowed transition, 1s → 3d). For NiPc, this peak was weak due to the high D_{4h} center of symmetry in the molecule, whereas the same feature was much more intense for O−Ni−N$_x$−GC suggesting hybridization of 3d and 4p orbitals of the Ni atoms, resulting in dipole-allowed 1s → 4p transitions to create more unpaired 3d electrons.[37−39] This hybridization was likely caused by distortions from D_{4h} symmetry, most probably due to the axial oxygen coordination disrupting the D_{4h} symmetry. The 1s → 4pz transition at ~8336 eV for O−Ni−N$_x$−GC was significantly less pronounced compared to the same peak for NiPc, again consistent with a distortion from the typical square planar Ni−N$_4$ structure, further evidencing the distorted D_{4h} symmetry of the Ni atoms in O−Ni−N$_x$−GC.[40,41] Fourier
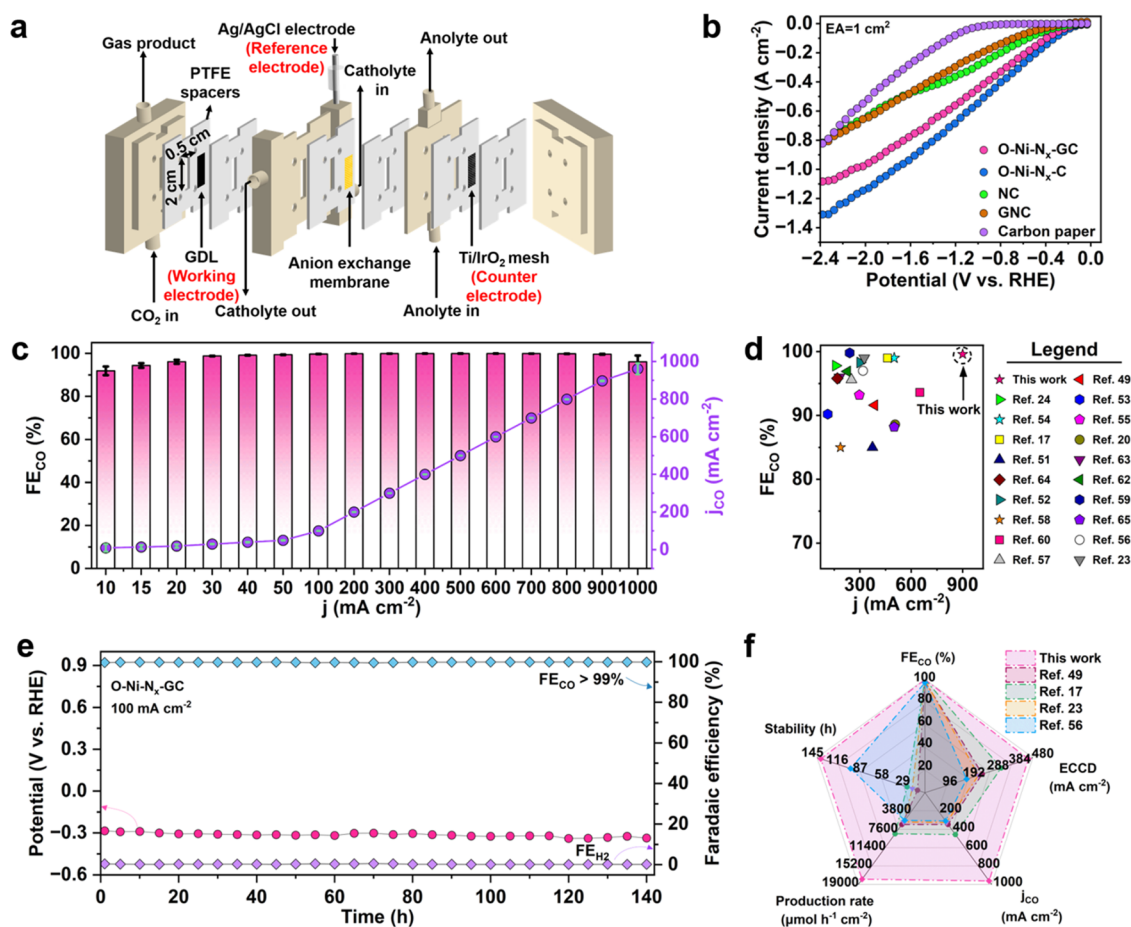
Figure 4. The CO$_2$RR performance of O−Ni−N$_x$−GC. (a) Schematic diagram of the GDE-based flow cell. (b) LSV curves for O−Ni−N$_x$−GC, O−Ni−N$_x$−C, GNC, and NC in 1 M KOH (the area of the GDE is 1 cm^{-2}, scan rate, 5 mV·s^{-1}). (c) FE$_{CO}$ and j$_{CO}$ for O−Ni−N$_x$−GC at different j values. (d) Comparison of the FE$_{CO}$ and maximum j values in a 1 M KOH electrolyte of recently reported state-of-the-art catalysts. (e) Durability tests of O−Ni−N$_x$−GC for CO$_2$RR at a current density of 100 mA·cm^{-2}. (f) Comparison of the stability, FE$_{CO}$, ECCD, CO production rate and partial current density to CO of O−Ni−N$_x$−GC and other state-of-the-art electrodes. Overall performance comparison between O−Ni−N$_x$−GC and reported state-of-the-art catalysts for CO$_2$-to-CO conversion. The error bars represent standard deviations of three measurements and the dashed lines are added guides to the eye. All measurements were conducted under the same conditions (1 M KOH, pH = 13.85, iR corrected 0.9 Ω, 25 °C).

transform-extended X-ray absorption fine structure (FT-EXAFS) spectra show a primary peak at ~1.4 Å (Figure 3b), attributable to the scattering interactions of Ni atoms with the first shell (Ni−N/O) in O−Ni−N$_x$−GC.[42] No Ni−Ni scattering path at ~2.1 Å was seen for O−Ni−N$_x$−C, confirming that Ni is atomically dispersed, consistent with HAADF-STEM and PXRD results. Next, bond lengths and coordination numbers were extracted from the optimized EXAFS curve fitting results to verify the coordination microenvironment around Ni atoms in O−Ni−N$_x$−GC (Figure 3c and Table S2).[42] These data supported the presence of a NiN$_4$−O (one axial O) active site in O−Ni−N$_x$−GC. The corresponding wavelet transform (WT)-EXAFS contour plot (Figure 3d) exhibited a strong WT signal at ~1.4 Å in R space, associated with Ni−N/O coordination in O−Ni−N$_x$−GC. The optimal average coordination numbers for O−Ni−N$_x$−GC was 4.86 (close to 5), with mean bond lengths of 1.96 Å, indicating the presence of five coordinated atoms around the nickel atoms, differing from the M-N$_4$ sites obtained from ZIF-8 reported previously (Table S2).[43−45]

Next, we carried out nitrogen sorption measurements at 77 K to study the porosity of O−Ni−N$_x$−GC. Type IV

adsorption−desorption isotherms were observed, suggesting the presence of layered micropore/mesoporous structures in the sample (Figure 3e). The Brunauer−Emmett−Teller (BET) surface area of O−Ni−N$_x$−GC was 746 m^2·g^{-1}. The CO$_2$ adsorption−desorption isotherms for O−Ni−N$_x$−GC were also measured up to 1 bar at 298 K (Figure 3f). The CO$_2$ uptake value is 53.8 cm^3·g^{-1} at 298 K, providing a basis for good CO$_2$ mass transfer. A water contact angle experiment showed that the water contact angle of O−Ni−N$_x$−GC is 138.8°, suggesting considerable hydrophobicity (Figure 3g). Taken together, these data strongly suggest the presence of an axial oxygen atom at NiN$_4$ sites in O−Ni−N$_x$−GC. On the basis of such NiN$_4$−O catalytic sites, high porosity, graphitic-N-rich carbon structural features, as well as excellent CO$_2$ uptake ability, O−Ni−N$_x$−GC possessed all the essential components to be a good electrocatalyst for CO$_2$-to-CO conversions, as was confirmed by the electrocatalytic experiments below. Moreover, the aforementioned structural characterizations of O−Ni−N$_x$−GC also provide solid experimental basis for subsequent density functional theory (DFT) modeling and mechanism studies of the CO$_2$RR.

To accurately assess the electrocatalytic CO_2RR performance of $O-Ni-N_x-GC$, we also synthesized graphitic N-rich porous carbon (denoted as GNC), N-doped carbon with a lower content of graphitic nitrogen (denoted as NC), and NC supporting atomically dispersed nickel with NiN_4-O sites (denoted as $O-Ni-N_x-C$). The synthesis and characterization data for these samples are provided in the Supporting Information (experimental section and material characterization). As expected, we found that GNC still exhibited a graphitic structure similar to $O-Ni-N_x-C$. SEM, PXRD, HAADF-STEM, and XAS revealed that $O-Ni-N_x-GC$ and NC also had similar structures as $O-Ni-N_x-GC$ and GNC, except with lower graphitic-N contents, respectively (Figures S7−S14, Tables S1 and S2).

Electrocatalytic CO_2RR Performance. To evaluate the electrocatalytic CO_2RR ability of the aforementioned catalysts, a traditional three-electrode setup was employed and applied in a flow cell device equipped with a gas diffusion electrode (GDE). The synthesized catalytic materials were coated on carbon papers to form working electrodes, with Ag/AgCl and Ti/IrO$_2$ used as reference and counter electrodes, respectively (Figure 4a). A 1 M KOH aqueous solution was used as the electrolyte, and a peristaltic pump used to circulate the solution through the anode and cathode compartments. Considering the impact of CO_2 consumption during the reaction, real-time monitoring of the gas outlet flow was achieved using an electronic soap bubble flowmeter to enhance the precision of Faradaic efficiency analysis.[46] Concurrently, a constant current method based on transient electrochemical technology was utilized for convenience and accuracy of current measurement at the working electrode. The linear sweep voltammetry (LSV) curves revealed that $O-Ni-N_x-GC$ and $O-Ni-N_x-C$ exhibited a significantly higher current response for CO_2 reduction than GNC and NC (Figure 4b). Carbon paper demonstrated much lower activity than GNC and NC. The data suggests that the presence of atomically dispersed Ni markedly enhanced the CO_2 reduction activity. The higher metal content observed in $O-Ni-N_x-C$ compared to $O-Ni-N_x-GC$, as indicated by ICP-MS results (Table S1), accounts for the slightly higher current density observed in $O-Ni-N_x-C$ at the same applied potentials. Gas products were collected at the gas outlet of the flow cell using gas bags, and their components and concentrations analyzed offline by gas chromatography (GC). Liquid reduction products were analyzed using offline ^1H nuclear magnetic resonance (^1H NMR) spectroscopy. CO and H$_2$ were the only gaseous products identified, with no evidence found for any liquid products being formed (Figure S15). As shown in Figure 4c, $O-Ni-N_x-GC$ achieved a remarkable FE_{CO} of 91.9% at an ultralow onset potential of −0.12 V vs RHE (10 mA·cm^{-2}) and delivered >99% FE_{CO} at −0.18 V vs RHE (overpotential ∼80.9 mV, with iR correction; 30 mA·cm^{-2}). In comparison, $O-Ni-N_x-C$ exhibited a 88.5% FE_{CO} at −0.12 V vs RHE and >99% FE_{CO} at −0.26 V vs RHE (overpotential ∼159.8 mV, with iR correction) (Table S3 and Figure S16). Notably, $O-Ni-N_x-GC$ was more effective in suppressing the hydrogen evolution reaction (HER) compared to $O-Ni-N_x-C$ across a wide range of current densities (Figure S17). Impressively, $O-Ni-N_x-GC$ demonstrated an excellent FE_{CO} (>99%) across a broad current density range from 100 to 900 mA·cm^{-2}, with FE_{H_2} values close to 0% over the same potential range. At a higher current density of 1 A·cm^{-2}, $O-Ni-N_x-GC$ exhibited a FE_{CO} of >96%, higher than that of $O-Ni-N_x-C$ (Figures 4c

and S16). The maximum j_{CO} values for $O-Ni-N_x-GC$ and $O-Ni-N_x-C$ were 960.5 and 944.1 mA·cm^{-2}, respectively, thus satisfying industrial-scale current density requirements (Table S4). Such performance exceeds all other previously reported CO_2-to-CO electrocatalysts in 1 M KOH (Figure 4d and Table S4), making both catalysts (especially $O-Ni-N_x-GC$) promising candidates for industrial-scale electrocatalytic CO_2 reduction. Moreover, CO production rates of 17916.51 and 17609.75 μmol·h^{-1}·cm^{-2} were realized for $O-Ni-N_x-GC$ and $O-Ni-N_x-C$, respectively, at a current density of 1 A·cm^{-2} (Figure S18). On the basis of atomically dispersed nickel sites, the calculated TOF values for $O-Ni-N_x-GC$ and $O-Ni-N_x-C$ were 81.5 s^{-1} and 24.0 s^{-1}, respectively (Figure S19 and Table S4). $O-Ni-N_x-GC$ thus showed a TOF value 3.3 times higher than that of $O-Ni-N_x-C$, providing substantial evidence efficiency of NiN_4-O sites on the highly graphitized-N doped porous carbon capsules for driving CO_2RR. To the best of our knowledge, this number is a record value as it exceeds the TOF value at ampere-level current densities of all Ni−N−C catalysts reported to date, such as Ni−N$_5$−C single-atom nanozyme (total current density of 1230 mA·cm^{-2}, TOF of 69.4 s^{-1}),[9] as well as Ni$_1$−N−C-50 carbon-based single atoms synthesized via microwave method on a ZIF-8 substrate (total current density of ∼1104 mA·cm^{-2}, TOF of ∼66.9 s^{-1}).[47] Next, the performance of $O-Ni-N_x-GC$ was assessed using the energy conversion current density (ECCD), a parameter that encapsulates energy conversion efficiency, product selectivity, and current density. The ECCD approach enables meaningful comparisons between catalysts and is a reliable measure of catalytic performance and selectivity.[9] The ECCD was calculated to be 460.4 mA·cm^{-2} at 1 A·cm^{-2} for $O-Ni-N_x-GC$, a record value that surpasses all other reported known electrocatalysts under similar conditions (Table S4 and Figure S20). Durability is a further important criterion when evaluating catalysts. Hence, we carried out constant current stability tests on $O-Ni-N_x-GC$ during CO_2RR at current densities of 100 and 200 mA·cm^{-2}, respectively. As shown in Figure 4e, $O-Ni-N_x-GC$ delivered a stable FE_{CO} close to 100% stable over 140 h of testing at a current density of 100 mA·cm^{-2}. At a current density of 200 mA·cm^{-2}, over 98% FE_{CO} was maintained for 34 h (Figure S21). The decreased FE_{CO} during the test is attributed to the reaction between the KOH electrolyte and CO_2 ($CO_2 + OH^- \rightarrow HCO_3^-$, $CO_2 + 2OH^- \rightarrow CO_3^{2-} + H_2O$),[48] which created carbonate/bicarbonate precipitates that disrupted the hydrophobic layer of the carbon paper, ultimately resulting in flooding. PXRD analysis of the $O-Ni-N_x-GC$ catalyst after the long-term durability test revealed that besides the characteristic peaks of accumulated salt crystals and the microporous layer of the carbon paper (Figure S22), there were no characteristic peaks of Ni crystallites, indicating that the single Ni atoms remained well-dispersed without aggregation. TEM images of $O-Ni-N_x-GC$ after stability tests demonstrate that the hollow structure did not collapse after 100 and 34 h at current densities of 100 and 200 mA·cm^{-2}, respectively (Figure S23). This verifies that the decline in catalytic performance was due to flooding rather than the catalyst itself, further demonstrating the exceptional durability of $O-Ni-N_x-GC$ in CO_2RR. Comparing the overall electrocatalytic CO_2-to-CO conversion performance such as FE_{CO}, ECCD, j_{CO}, production rate, and durability, it is evident that $O-Ni-N_x-GC$ outperforms other previously reported electrocatalysts in 1 M KOH electrolyte,
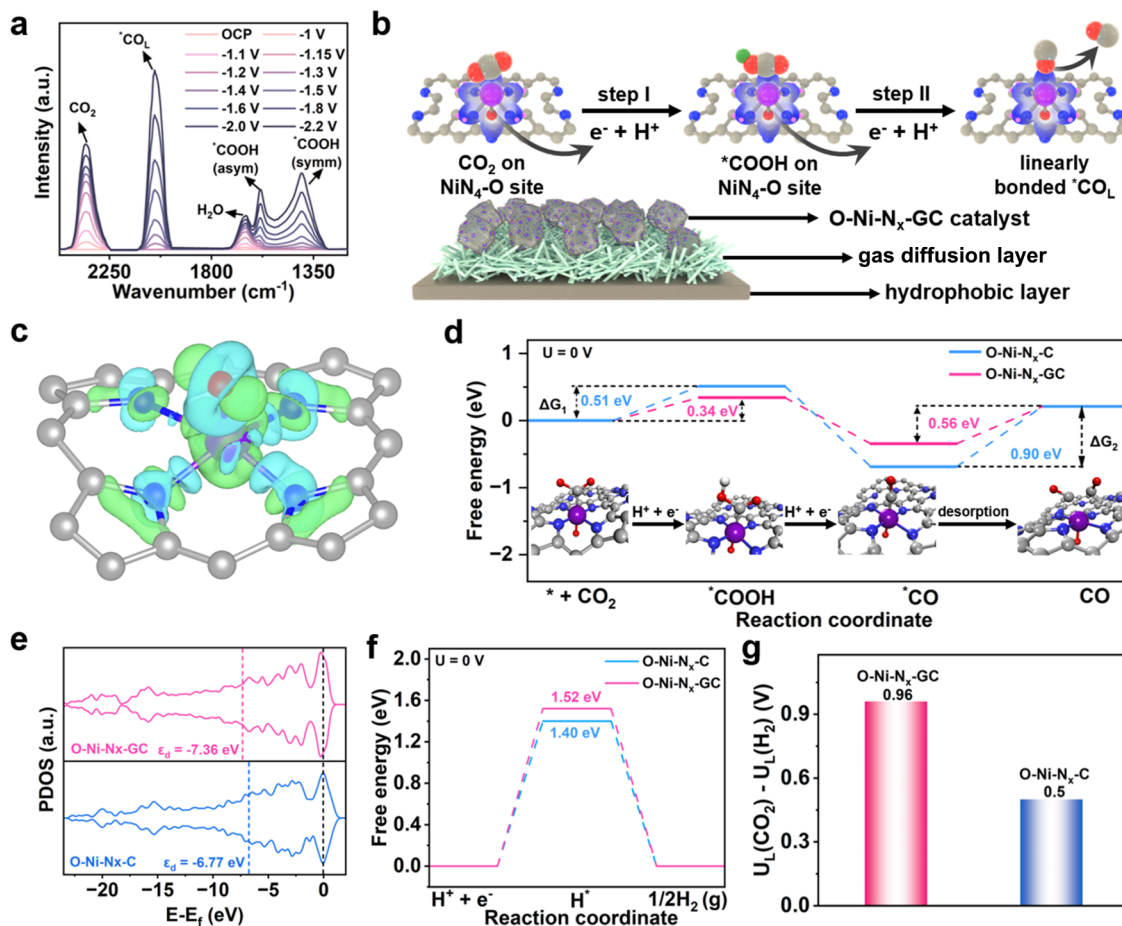
Figure 5. *In-situ* ATR-SEIRAS experiment and DFT calculation. (a) *In-situ* ATR-SEIRAS spectra of O−Ni−N_x−GC at different potentials in a 1 M KOH electrolyte. (b) Schematic illustration of the CO_2RR mechanism in the flow cell system. (c) The charge density difference of O−Ni−N_x−GC, with an iso-surface level of 0.005 e bohr^{-3} (the Cyan and green regions indicate electron accumulation and depletion, respectively). (d) Free energy diagram of CO_2RR on NiN_4−O active site at U = 0 V (inset shows the DFT model of O−Ni−N_x−GC adsorbing CO_2, *COOH, and *CO, and desorbing CO). (e) Projected d-density of states of Ni over O−Ni−N_x−GC and O−Ni−N_x−C surfaces. (f) Free energy diagram of HER on O−Ni−N_x−GC and O−Ni−N_x−C at U = 0 V. (g) Limiting potential differences for CO_2RR and HER on O−Ni−N_x−GC and O−Ni−N_x−C at U = 0 V.

positioning it as an excellent candidate for industrial-scale electrocatalytic CO_2RR (Figure 4f and Table S4).[9,17−20,23,24,48−65]

Electrocatalytic CO_2RR Mechanism. To further elucidate the electrocatalytic CO_2RR mechanism of O−Ni−N_x−GC, we conducted *in situ* attenuated total reflectance-surface-enhanced infrared absorption spectroscopy (ATR-SEIRAS) measurements in a 1 M KOH aqueous solution. Potential-dependent ATR-SEIRAS spectra were obtained from −1 to −2.2 V vs Ag/AgCl, using the infrared spectra obtained at open circuit voltage as the baseline. Signals corresponding to CO_2 adsorption and interfacial H_2O (H−O−H bending vibration) appeared at around 2355 and 1647 cm^{-1}, respectively (Figure 5a). With an increase in potential, the signal of adsorbed CO_2 gradually intensified. Meanwhile, the concurrent enhancement of the interfacial H_2O signal would promote the hydrogenation of adsorbed CO_2, accelerating the formation of the *COOH intermediate and thus improving the efficiency of CO_2 reduction. This suggests that CO_2 adsorption and activation are enhanced at higher potentials. The concomitant enhancement of the interfacial H_2O peak signal will facilitate the hydrogenation of adsorbed CO_2, expediting the generation of *COOH intermediates, and thereby improves the efficiency of

CO_2 reduction.[56] The high-frequency bands above 1800 cm^{-1} originate from CO adsorption on metal binding sites.[66] The peak around 2050 cm^{-1} is typical for linearly bonded *CO_L (adsorbed CO, Ni−C≡O). No bridge-bonded *CO_B adsorption was detected, and there was no shift in the *CO_L signal position with increasing CO coverage, indicating the absence of any interaction between adsorbed CO molecules, confirming once again the atomic dispersion of Ni active sites.[51,67] The signal for *CO_L gradually intensified with increasing voltage, consistent with experimental results. Two peaks were observed near 1405 and 1581 cm^{-1}, attributed to the symmetric stretching (C=O) and asymmetric stretching (C−O) of surface *COOH intermediates, recognized as a key intermediate in the generation of CO.

Additionally, we conducted time-dependent ATR-SEIRAS spectroscopy measurements and recorded the infrared spectra of O−Ni−N_x−GC at −1.3 V (Figure S24). At 30 s, *COOH and *CO_L were detected, indicating that the adsorbed CO_2 molecules were rapidly converted to *COOH. Additionally, the signal of each characteristic peak intensified with extending the electrolysis time. Therefore, we propose a reaction pathway involving three steps (Figure 5b). First, a CO_2 molecule adsorbs onto the single-Ni-atom centers, forming *COOH

intermediates through proton-coupled electron transfer (PCET, step I).[68] Subsequently, addition of a further electron and a proton yields *CO and H_2O (step II). Finally, the last step involves the desorption of *CO from the catalyst surface, resulting in gaseous CO production.

Subsequently, DFT calculations were conducted to gain a deeper understanding of the superior CO_2RR catalytic activity of the O−Ni−N_x−GC catalyst. Models for O−Ni−N_x−GC and O−Ni−N_x−C were established and optimized based on the above structure characterization data. As shown in Figure 5c, the charge density difference analyses for O−Ni−N_x−GC and O−Ni−N_x−C reveal that, unlike the traditional Ni−N_4 coordination,[69] electrons in both samples are transferred not only to the N atom but also to the axial O, significantly enhancing electron delocalization at the Ni center and reducing the energy barrier of the rate-determining step (RDS) in CO_2RR.[70] Furthermore, Gibbs free energy calculations (Figure 5d) indicate that, at $U = 0$ V, the ΔG_1 ($CO_2 + * \rightarrow$ *COOH) on O−Ni−N_x−GC is 0.34 eV, significantly lower than that on O−Ni−N_x−C (0.51 eV), suggesting that *COOH is more stably adsorbed on the highly graphitized O−Ni−N_x−GC catalyst, facilitating the production of CO at lower potentials. With the aid of PCET, the ΔG for the dissociation of *COOH to form *CO and H_2O was shown to be downhill on both catalyst models. Moreover, the desorption energy barrier (ΔG_2, *CO → CO + *) of O−Ni−N_x−GC (0.56 eV) for *CO was much lower than that of O−Ni−N_x−C (0.90 eV), explaining the higher selectivity of O−Ni−N_x−GC toward CO. These theoretical results agree well with the experimental results. The ΔG_2 was higher than ΔG_1 on both materials at $U = 0$ V, and when $U = -0.3$ V, the ΔG_1 decreased for both materials, favoring CO_2RR, while the nonelectrochemical step of CO desorption, ΔG_2, remained constant in both models (Figure S25). However, ΔG_1 remained lower than ΔG_2, indicating that the desorption of *CO is the RDS, which explains the presence of *CO signals in the in situ ATR-SEIRAS experiments. Thus, the in situ ATR-SEIRAS results and DFT calculations confirm the presence of *COOH and *CO intermediates on the electrocatalyst surface, consistent with the assumed ECR pathway. Additionally, the projected density of states (PDOS) of the Ni-3d orbitals for O−Ni−N_x−C and O−Ni−N_x−GC were calculated (Figure 5e). Compared to O−Ni−N_x−C, the d-band center of the Ni-3d orbital of O−Ni−N_x−GC shifts toward the negative state as the degree of graphitization increases. This shift weakens the adsorption of *CO intermediates on O−Ni−N_x−GC, thereby enhancing the selectivity for CO.

Considering that HER is the main side reaction of CO_2RR, the difference in the thermodynamic limiting potentials ($U_{L(CO2)} - U_{L(H2)}$, ΔU_L) for CO_2RR and HER ($U_L = -\Delta G/e$) was calculated on each catalyst to determine the competition and selectivity of the reactions.[55,71] Based on the free energy diagrams of CO_2RR and HER (Figure 5d,f), the relevant thermodynamic limiting potentials are shown in Figure 5g. Generally, a higher positive ΔU_L indicates a higher selectivity for CO_2RR. As expected, compared to O−Ni−N_x−C, O−Ni−N_x−GC with a highly graphitized structure exhibited the more positive ΔU_L value (0.84 V). Utilizing these structures, the Gibbs free energy with graphitic-N as the catalytic site was calculated. As expected, compared to O−Ni−N_x−C, graphitic-N in the O−Ni−N_x−GC structure was found to more effective in reducing the energy barrier of the RDS (Figure S26). Moreover, graphitic-N site on O−Ni−N_x−GC

demonstrated a higher HER free energy than for O−Ni−N_x−C, suggesting that O−Ni−N_x−GC is more capable of suppressing hydrogen evolution reactions (Figure S27). These results are highly consistent with the experimental observations of GNC exhibiting optimal FE_{CO} performance and enhanced selectivity for CO generation (Figures S28 and S29). On the basis of experimental results and theoretical calculations, we conclude that the active sites enriched with graphitic-nitrogen enable the O−Ni−N_x−GC catalyst to deliver excellent CO_2RR activity while suppressing the competitive HER. The exceptional electrocatalytic activity of O−Ni−N_x−GC for the reduction of CO_2-to-CO is based on its unique axial oxygen coordination NiN_4−O structure and supplemented by the catalytic effect of graphitic-N, which contributes to better ΔG values for *COOH formation and *CO desorption.

Taken together, the aforementioned experimental and theoretical results demonstrate that the combination of atomically dispersed nickel (coordinated by 4 in-plane N atoms and axial oxygen) and graphitic N-rich porous carbon support creates a very effective electrocatalyst for CO_2 reduction. The presence of NiN_4−O active sites with graphitic-N species synergistically reduce the activation energy barrier for CO_2 adsorption and promotes the formation of intermediate *COOH. It also facilitates *CO desorption from O−Ni−N_x−GC capsules, improving the electrocatalytic CO_2-to-CO conversion performance and avoiding hydrogen evolution. In addition, the high porosity of the porous carbon capsules allows efficient mass transport, resulting in fast CO_2 adsorption on NiN_4−O active sites, together with quick reduction to a CO product. Further, the relationship between the O−Ni−N_x−GC structure and their CO_2 reduction performance has been clearly identified at a molecular level. We anticipate that our proof-of-concept study will promote the synthesis of improved metal−nitrogen−carbon catalysts for electrocatalytic CO_2 reduction and other target applications.

CONCLUSIONS

In conclusion, atomically dispersed nickel (with a NiN_4−O coordination) on a graphitic N-rich porous carbon support (denoted herein as O−Ni−N_x−GC) delivers excellent CO_2-to-CO conversion performance over a wide range of current densities (0.01 to 1 A·cm^{-2}). The Faradaic efficiencies achieved (~100% FE_{co}) surpass the performance of most previously reported metal−nitrogen−carbon catalysts, especially at low overpotential and ampere-level current densities. Experimental and theoretical calculations indicated that the presence of abundant graphitic-N close to the NiN_4−O active sites in O−Ni−N_x−GC not only lowered the energy barrier for *COOH production and the desorption of *CO, but also suppressed the competitive hydrogen evolution reaction. Our findings not only offer new vistas for the design of atomically dispersed catalysts for CO_2RR, but also underscore the regulatory capability of graphitic-N in modulating the catalytic performance of metal active sites, which holds significant implications for the future development of CO_2-to-CO electrocatalysts.

METHODS

Synthesis of ZIF-8, ZIF-8@K-TA, and ZIF-8@Ni-TA Nanocrystals. ZIF-8 nanocrystals were synthesized using a reported procedure with a slight modification.[72] In a typical synthesis, 4.1 g of 2-methylimidazole was dissolved in 60 mL of MeOH to form a clear

solution. Next, 1.58 g of $Zn(NO_3)_2 \cdot 6H_2O$ was then added into the 2-methylimidazole solution followed by vigorous stirring for 1 h. The mixture was then incubated at room temperature without stirring. After 24 h, the product was isolated as a white powder by centrifugation and washed several times with MeOH, and finally dried overnight under vacuum (yielding ZIF-8 nanocrystals).

Next, 250 mg of ZIF-8 nanocrystals were dispersed in deionized water by sonication for 10 min. Then, a tannic acid solution (24 mM, 10 mL) of pH = 8 (adjusted by adding 6 M KOH aqueous solution) was added to the ZIF-8 dispersion under constant stirring. After stirring for 5 min, the solid product was collected by centrifugation, and washed several times with deionized water and MeOH, yielding ZIF-8@K-TA.

Subsequently, 200 mg of nickel nitrate hydrate $(Ni(NO_3)_2 \cdot 6H_2O)$ was dissolved in 150 mL of MeOH under stirring for 10 min. Then, the obtained ZIF-8@K-TA was added to the nickel nitrate solution, with the resulting dispersion being stirred for 3 h at room temperature. The solid product was collected by centrifugation and washed several times with MeOH. Finally, the product was dried in an oven at 40 °C under vacuum to yield ZIF-8@Ni-TA.

Synthesis of Hollow O−Ni−N$_x$−GC, O−Ni−N$_x$−C, NC, and GNC Capsules. ZIF-8@Ni-TA was placed in a tube furnace and heated to 1000 °C (3 °C/min) under an argon atmosphere. After annealing at 1000 °C for 3 h, the black powder sample was cooled to room temperature and then immersed in 3 M HCl at 120 °C for 12 h, followed by washing with deionized water. After being dried at 75 °C in a vacuum oven, the powder was again heat-treated at 1000 °C for 3 h under an argon atmosphere to obtain O−Ni−N$_x$−GC. GNC was synthesized using the same heating protocol using the ZIF-8@K-TA precursor. O−Ni−N$_x$−C and NC were prepared via similar synthetic routes (using a lower pyrolysis temperature of 900 °C) from ZIF-8@Ni-TA and ZIF-8@K-TA precursors, respectively.

Carbon Dioxide Electroreduction Reaction Measurements. All electrochemical measurements were conducted using a CHI 1140D potentiostat at 25 °C. The measurement potentials were manually corrected using the iR compensation function of the potentiostat to extract the actual working potential of the cathode for comparison with other catalysts (∼0.9 Ω resistance). All potentials were calibrated to the reversible hydrogen electrode (RHE) and converted using the formula:

$$E_{\text{RHE}} = E_{\text{Ag/AgCl}} + 0.0591 \times \text{pH} + 0.197\ \text{V} - iR_{\text{u}}$$

where i is the applied current and R_{u} is the solution resistance.

Gas products were analyzed using a gas chromatograph (FULI GC9790PLUS) and the liquid products were detected using Bruker Avance III HD 500 MHz nuclear magnetic resonance (NMR). The gas chromatograph was equipped with both a packed molecular sieve 5A column and a HAYESEP-A column, with high-purity argon (99.999%) serving as the carrier gas. Quantification of the CO fraction was performed using a flame ionization detector (FID) equipped with a nickel conversion furnace, while the H$_2$ fraction was quantified using a thermal conductivity detector (TCD). The standard curves for CO and H$_2$ are shown in Figure S30. The reported FEs represented average values derived from a minimum of three measurements. Faradaic efficiency was calculated as follows:

$$\text{FE (\%)} = \frac{Q_{\text{gas}}}{Q_{\text{total}}} = \frac{V \times t \times \nu\frac{\%}{V_{\text{m}}} \times N \times F}{i_{\text{total}} \times t}$$

$$= \frac{V \times \nu\frac{\%}{V_{\text{m}}} \times N \times F}{i_{\text{total}} \times 60(\text{s min}^{-1})} \times 100\%$$

Q: charge number.
V: the flow rate of CO$_2$ (s.c.c.m).
ν (%): the measured gas product concentration in the GC sample loop.
V_{m}: the molar volume of gas: 24 L·mol^{-1}.
N: the number of electron transferred for product formation, which is 2 for CO.

F: Faradaic constant, 96,500 C·mol^{-1}.
i_{total}: the total current.

The experiment was conducted in a flow cell reactor equipped with a gas diffusion electrode (GDE, Gaossunion 101017-1), with an electrolysis window of 2×0.5 cm^2, resulting in an effective area of 1 cm^2. A conventional three-electrode configuration was employed for CO$_2$RR measurements, with the cathode consisting of a gas diffusion layer (GDL, YLS-30T, from Suzhou Sinero, China), the anode composed of IrO$_2$−Ti mesh (2×0.5 cm^2, 1 mg·cm^{-2}, 0.1 mm thickness, from Kunshan Yiwanlin Electronic Technology Co., Ltd.), and the Ag/AgCl reference electrode (filled with saturated KCl solution) placed in the cathode compartment. The cathode and anode compartments were separated by an anion exchange membrane (Fumasep FAB-PK-130). During the preparation of the GDE, 5 mg of catalyst was mixed with 50 μL of a 5 wt % Nafion solution, 475 μL of ethanol, and 475 μL of deionized water, and sonicated for 2 h at 25 °C. The obtained catalyst ink was carefully sprayed onto a commercial Sigracet GDL with dimensions of 2.3×0.8 cm^2 (actual working area: 2×0.5 cm^2) to achieve a catalyst loading of 1 mg cm^{-2}. The geometric area of the electrode was used to calculate all current densities. A double-sided copper foil tape (0.05 mm thick, 10 mm wide) was used as the current collector for the cathode. After drying the GDE overnight at room temperature, it was integrated into the flow cell with the side of the cathode coated with the catalyst facing the electrolyte. A high-purity CO$_2$ gas (99.999%) was supplied directly to the GDE cathode at a rate of 90 s.c.c.m (as measured by a soap film flow meter). The cathodic electrolyte composed of 1 M KOH was continuously circulated through the cathode chamber at a flow rate of 5 s.c.c.m using a peristaltic pump. For CO$_2$ reduction product detection experiments, the catalyst was initially activated by electrolysis at 10 mA for 30 min. Subsequently, the electrode was operated in constant current mode (potentiostatic measurements), with each current applied for 10 min to obtain Faradaic efficiencies at different current densities. The potential was recorded after the applied current reached a stable state. Gas collection was performed using a gas bag after reaction for ten min. Furthermore, considering the reduction in the outlet gas flow rate caused by the consumption of CO$_2$ during the cathodic reaction process and the neutralization of CO$_2$ by KOH, the outlet gas flow rate was monitored in real-time using a soap film flow meter to accurately quantify the Faradaic efficiencies of CO and H$_2$. During the stability test, electrolysis was periodically paused, and the electrode cleaned to prevent the loss of GDE hydrophobicity and to mitigate flooding over time.

The turnover frequency (TOF, h^{-1}) for CO generation was calculated as follows:

$$\text{TOF} = \frac{j_{\text{CO}}/n \times F}{\omega \times m_{\text{catalyst}}/M_{\text{metal}}}$$

j_{CO}: partial current of CO.
ω: the content of Ni in the catalyst acquired from ICP-MS.
m_{catalyst}: the catalyst loading (1 mg·cm^{-2}).
M_{metal}: the atomic mass of Ni (58.69 g·mol^{-1}).
The cathodic energy conversion efficiency (ECE, %) and energy conversion current density (ECCD, mA·cm^{-2}) in the flow cell were calculated as follows:

$$\text{ECE} = \frac{E_{\text{cell}} \times \text{FE}_{\text{CO}}}{1.23 - E_{\text{applied}}}$$

$$\text{ECCD} = \frac{E_{\text{cell}} \times j_{\text{CO}}}{1.23 - E_{\text{applied}}}$$

E_{cell}: thermodynamic cell potential between cathode and anode reactions, which is $E_{\text{cell}} = -1.23\ \text{V} - (-0.1\ V) = 1.33\ \text{V}$, where -0.1 V vs RHE represents the thermodynamic cell potential of CO, and 1.23 V vs RHE represents the thermodynamic cell potential of water oxidation.

E_{applied}: the applied potential.

***In-Situ* ATR-SEIRAS Measurements.** *In-situ* attenuated total reflection surface-enhanced infrared absorption spectroscopy (ATR-SEIRAS) measurements were conducted on a Nicolet iS50 FTIR spectrometer. Diamond-like carbon was coated onto silicon chips (5 × 8 × 1 mm³) to prepare internal reflection elements (IRE). Prior to the experiments, the coated IRE was ultrasonically treated with 30 wt % concentrated H_2SO_4 for 2 min, followed by rinsing with deionized water. Catalyst ink (1 mg·mL^{-1} in ethanol/Nafion/H_2O) was dropped onto the IRE and left to dry in air at room temperature. Glassy carbon paper was placed on top of the catalyst layer to ensure good electrical contact. A glassy carbon rod, Pt mesh, and Ag/AgCl in 3 M KCl were connected to the IRE as the working electrode, counter electrode, and reference electrode, respectively. *In-situ* ATR-SEIRAS measurements were performed using an FTIR spectrometer equipped with a mercury cadmium telluride (MCT) detector. During the recording of infrared spectra, a Gamry Reference 600 potentiostat was utilized.

Computational Methods. The first-principles calculations within the framework of density functional theory (DFT),[73−76] including structural and energetic performances, were carried out based on the Dmol³ module in Materials Studio 2020.[77] The generalized gradient approximation (GGA) function was implemented in the Perdew−Burke−Ernzerhof (PBE) exchange correlation function.[78,79] The basic set of the double numerical plus polarization (DNP) and the DFT-D method for van der Waals dispersion corrections with the TS scheme were employed to describe the occupied molecular orbital expansion and to measure electrostatic interactions accurately, respectively. The convergence criteria for electronic energy, max displacement and max force on each atom were set to be 10^{-5} Ha, 0.005 Å and 0.002 Ha·Å^{-1}, respectively.

Gibbs free energy change in each elementary step of the CO_2 reduction reaction and hydrogen evolution reaction could be calculated according to the following equation:

$$\Delta G = \Delta E + \Delta ZPE - T\Delta S - \Delta G_U$$

in which ΔZPE, T, and ΔS represent the change of the zero-point energy, temperature (298.15 K), and the change of entropy, respectively. $\Delta G_U = -eU$.

Charge density difference calculations are performed in the framework of the density functional theory with the projector augmented plane-wave method, as implemented in the Vienna *ab initio* simulation package.[80] Spin polarization was also included. The cutoff energy for the plane wave was set to 450 eV. The energy criterion is set to 1 × 10^{-06} eV in the iterative solution of the Kohn−Sham equation. The electron smearing width of σ = 0.03 eV was employed according to the Gaussian smearing technique.

The charge density difference was evaluated using the formula $\Delta\rho = \rho(\text{slab}) - \rho(\text{slab-atom}) - \rho(\text{atom})$, then analyzed by using the VESTA code.[81]

ASSOCIATED CONTENT

ⓢ Supporting Information

The Supporting Information is available free of charge at https://pubs.acs.org/doi/10.1021/acsnano.4c14192.

Materials and measurements, scheme of the experimental setup, additional materials characterization (FTIR, PXRD, TGA, SEM, XPS, NMR, Raman, TEM, HRTEM, XANES, EXAFS, GC data, *in situ* ATR-SEIRAS spectra, gas sorption analysis, DFT calculations, and other electrochemical performance characterization of catalysts) (PDF)

AUTHOR INFORMATION

Corresponding Authors

Hui Yang − *College of Environmental Science and Engineering, North China Electric Power University, Beijing 102206, P. R. China*; Email: h.yang@ncepu.edu.cn

Shengqian Ma − *Department of Chemistry, University of North Texas, Denton, Texas 76201, United States;* ⓞ orcid.org/0000-0002-1897-7069; Email: shengqian.ma@unt.edu

Xiangke Wang − *College of Environmental Science and Engineering, North China Electric Power University, Beijing 102206, P. R. China;* ⓞ orcid.org/0000-0002-3352-1617; Email: xkwang@ncepu.edu.cn

Authors

Yichen Sun − *College of Environmental Science and Engineering, North China Electric Power University, Beijing 102206, P. R. China;* ⓞ orcid.org/0000-0001-8329-4507

Xiaolu Liu − *College of Environmental Science and Engineering, North China Electric Power University, Beijing 102206, P. R. China*

Jiazheng Tian − *College of Environmental Science and Engineering, North China Electric Power University, Beijing 102206, P. R. China*

Zixuan Zhang − *College of Environmental Science and Engineering, North China Electric Power University, Beijing 102206, P. R. China*

Yang Li − *College of Environmental Science and Engineering, North China Electric Power University, Beijing 102206, P. R. China*

Yinghui Xie − *College of Environmental Science and Engineering, North China Electric Power University, Beijing 102206, P. R. China*

Mengjie Hao − *College of Environmental Science and Engineering, North China Electric Power University, Beijing 102206, P. R. China*

Zhongshan Chen − *College of Environmental Science and Engineering, North China Electric Power University, Beijing 102206, P. R. China*

Geoffrey I. N. Waterhouse − *School of Chemical Sciences, The University of Auckland, Auckland 1142, New Zealand;* ⓞ orcid.org/0000-0002-3296-3093

Complete contact information is available at:
https://pubs.acs.org/10.1021/acsnano.4c14192

Author Contributions

H.Y., X.W., and S.M. conceived and designed the research. Y.S., X.L., J.T., Z.Z., Y.L., Y.X., and M.H. performed the synthesis and characterization and carried out the experiments. Y.S., X.L., and Z.C. performed and analyzed the TEM and DFT calculations. H.Y., X.W., G.I.N.W., and S.M. wrote the manuscript. All authors contributed to the discussion, and gave approval to the final version of the manuscript.

Notes

The authors declare no competing financial interest.

ACKNOWLEDGMENTS

REFERENCES

(1) De Luna, P.; Hahn, C.; Higgins, D.; Jaffer, S. A.; Jaramillo, T. F.; Sargent, E. H. What would it take for renewably powered electrosynthesis to displace petrochemical processes? *Science* **2019**, *364*, No. eaav3506.

(2) Costentin, C.; Drouet, S.; Robert, M.; Savéant, J.-M. A Local Proton Source Enhances CO_2 Electroreduction to CO by a Molecular Fe Catalyst. *Science* **2012**, *338*, 90−94.

(3) Gao, S.; Lin, Y.; Jiao, X.; Sun, Y.; Luo, Q.; Zhang, W.; Li, D.; Yang, J.; Xie, Y. Partially oxidized atomic cobalt layers for carbon dioxide electroreduction to liquid fuel. *Nature* **2016**, *529*, 68−71.

(4) Timoshenko, J.; Bergmann, A.; Rettenmaier, C.; Herzog, A.; Arán-Ais, R. M.; Jeon, H. S.; Haase, F. T.; Hejral, U.; Grosse, P.; Kühl, S.; et al. Steering the structure and selectivity of CO_2 electroreduction catalysts by potential pulses. *Nat. Catal.* **2022**, *5*, 259−267.

(5) Guo, W.; Tan, X.; Jia, S.; Liu, S.; Song, X.; Ma, X.; Wu, L.; Zheng, L.; Sun, X.; Han, B. Asymmetric Cu Sites for Enhanced CO_2 Electroreduction to C_{2+} Products. *CCS Chem.* **2024**, *6*, 1231−1239.

(6) Xu, A.; Hung, S.; Cao, A.; Wang, Z.; Karmodak, N.; Huang, J. E.; Yan, Y.; Sedighian Rasouli, A.; Ozden, A.; Wu, F.; et al. Copper/alkaline earth metal oxide interfaces for electrochemical CO_2-to-alcohol conversion by selective hydrogenation. *Nat. Catal.* **2022**, *5*, 1081−1088.

(7) Yang, H. B.; Hung, S.; Liu, S.; Yuan, K.; Miao, S.; Zhang, L.; Huang, X.; Wang, H.; Cai, W.; Chen, R.; et al. Atomically dispersed Ni(i) as the active site for electrochemical CO_2 reduction. *Nat. Energy* **2018**, *3*, 140−147.

(8) Nitopi, S.; Bertheussen, E.; Scott, S. B.; Liu, X.; Engstfeld, A. K.; Horch, S.; Seger, B.; Stephens, I. E. L.; Chan, K.; Hahn, C.; et al. Progress and Perspectives of Electrochemical CO_2 Reduction on Copper in Aqueous Electrolyte. *Chem. Rev.* **2019**, *119*, 7610−7672.

(9) Huang, J. R.; Qiu, X. F.; Zhao, Z. H.; Zhu, H. L.; Liu, Y. C.; Shi, W.; Liao, P. Q.; Chen, X. M. Single-Product Faradaic Efficiency for Electrocatalytic of CO_2 to CO at Current Density Larger than 1.2 A cm^{-2} in Neutral Aqueous Solution by a Single-Atom Nanozyme. *Angew. Chem., Int. Ed.* **2022**, *61*, No. e202210985.

(10) Wen, G.; Ren, B.; Wang, X.; Luo, D.; Dou, H.; Zheng, Y.; Gao, R.; Gostick, J.; Yu, A.; Chen, Z. Continuous CO_2 electrolysis using a CO_2 exsolution-induced flow cell. *Nat. Energy* **2022**, *7*, 978−988.

(11) Wu, Q.-J.; Si, D.-H.; Wu, Q.; Dong, Y.-L.; Cao, R.; Huang, Y.-B. Boosting Electroreduction of CO_2 over Cationic Covalent Organic Frameworks: Hydrogen Bonding Effects of Halogen Ions. *Angew. Chem., Int. Ed.* **2023**, *62*, No. e202215687.

(12) Jin, S.; Hao, Z.; Zhang, K.; Yan, Z.; Chen, J. Advances and Challenges for the Electrochemical Reduction of CO_2 to CO: From Fundamentals to Industrialization. *Angew. Chem., Int. Ed.* **2021**, *60*, 20627−20648.

(13) Bushuyev, O. S.; De Luna, P.; Dinh, C. T.; Tao, L.; Saur, G.; van de Lagemaat, J.; Kelley, S. O.; Sargent, E. H. What Should We Make with CO_2 and How Can We Make It? *Joule* **2018**, *2*, 825−832.

(14) Liu, Z.; Cao, L.; Wang, M.; Zhao, Y.; Hou, M.; Shao, Z. A robust Ni single-atom catalyst for industrial current and exceptional selectivity in electrochemical CO_2 reduction to CO. *J. Mater. Chem. A* **2024**, *12*, 8331−8339.

(15) Wang, T.; Wang, J.; Lu, C.; Jiang, K.; Yang, S.; Ren, Z.; Zhang, J.; Liu, X.; Chen, L.; Zhuang, X.; Fu, J. Single-Atom Anchored Curved Carbon Surface for Efficient CO_2 Electro-Reduction with Nearly 100% CO Selectivity and Industrially-Relevant Current Density. *Adv. Mater.* **2023**, *35*, No. 2205553.

(16) Feng, J.; Gao, H.; Zheng, L.; Chen, Z.; Zeng, S.; Jiang, C.; Dong, H.; Liu, L.; Zhang, S.; Zhang, X. A Mn-N_3 single-atom catalyst embedded in graphitic carbon nitride for efficient CO_2 electroreduction. *Nat. Commun.* **2020**, *11*, 4341.

(17) Zhao, R.; Wang, Y.; Ji, G.; Zhong, J.; Zhang, F.; Chen, M.; Tong, S.; Wang, P.; Wu, Z.; Han, B.; Liu, Z. Partially Nitrided Ni Nanoclusters Achieve Energy-Efficient Electrocatalytic CO_2 Reduction to CO at Ultralow Overpotential. *Adv. Mater.* **2023**, *35*, No. 2205262.

(18) Wang, X.; Sang, X.; Dong, C.; Yao, S.; Shuai, L.; Lu, J.; Yang, B.; Li, Z.; Lei, L.; Qiu, M.; et al. Proton Capture Strategy for Enhancing Electrochemical CO_2 Reduction on Atomically Dispersed Metal-Nitrogen Active Sites**. *Angew. Chem.* **2021**, *133*, 12066−12072.

(19) Chen, K.; Cao, M.; Lin, Y.; Fu, J.; Liao, H.; Zhou, Y.; Li, H.; Qiu, X.; Hu, J.; Zheng, X.; et al. Ligand Engineering in Nickel Phthalocyanine to Boost the Electrocatalytic Reduction of CO_2. *Adv. Funct. Mater.* **2022**, *32*, No. 2111322.

(20) Chen, Z.; Zhang, X.; Liu, W.; Jiao, M.; Mou, K.; Zhang, X.; Liu, L. Amination strategy to boost the CO_2 electroreduction current density of M-N/C single-atom catalysts to the industrial application level. *Energy Environ. Sci.* **2021**, *14*, 2349−2356.

(21) Sun, Y.; Liu, X.; Zhu, M.; Zhang, Z.; Chen, Z.; Wang, S.; Ji, Z.; Yang, H.; Wang, X. Non-noble metal single atom-based catalysts for electrochemical reduction of CO_2: Synthesis approaches and performance evaluation. *DeCarbon* **2023**, *2*, No. 100018.

(22) Wu, Y.; Chen, C.; Yan, X.; Sun, X.; Zhu, Q.; Li, P.; Li, Y.; Liu, S.; Ma, J.; Huang, Y.; Han, B. Boosting CO_2 Electroreduction over a Cadmium Single-Atom Catalyst by Tuning of the Axial Coordination Structure. *Angew. Chem., Int. Ed.* **2021**, *60*, 20803−20810.

(23) Li, X.; Han, S.; Wu, W.; Zhang, K.; Chen, B.; Zhou, S.; Ma, D.; Wei, W.; Wu, X.; Zou, R.; Zhu, Q. L. Convergent paired electrosynthesis of dimethyl carbonate from carbon dioxide enabled by designing the superstructure of axial oxygen coordinated nickel single-atom catalysts. *Energy Environ. Sci.* **2023**, *16*, 502−512.

(24) Wang, C.; Wang, X.; Ren, H.; Zhang, Y.; Zhou, X.; Wang, J.; Guan, Q.; Liu, Y.; Li, W. Combining Fe nanoparticles and pyrrole-type Fe-N_4 sites on less-oxygenated carbon supports for electrochemical CO_2 reduction. *Nat. Commun.* **2023**, *14*, No. 5108.

(25) Gong, Y. N.; Cao, C. Y.; Shi, W. J.; Zhang, J. H.; Deng, J. H.; Lu, T. B.; Zhong, D. C. Modulating the Electronic Structures of Dual-Atom Catalysts via Coordination Environment Engineering for Boosting CO_2 Electroreduction. *Angew. Chem., Int. Ed.* **2022**, *61*, No. e202215187.

(26) Yang, H.; Lin, Q.; Zhang, C.; Yu, X.; Cheng, Z.; Li, G.; Hu, Q.; Ren, X.; Zhang, Q.; Liu, J.; He, C. Carbon dioxide electroreduction on single-atom nickel decorated carbon membranes with industry compatible current densities. *Nat. Commun.* **2020**, *11*, No. 593.

(27) Xi, D.; Li, J.; Low, J.; Mao, K.; Long, R.; Li, J.; Dai, Z.; Shao, T.; Zhong, Y.; Li, Y.; et al. Limiting the Uncoordinated N Species in M-Nx Single-Atom Catalysts toward Electrocatalytic CO_2 Reduction in Broad Voltage Range. *Adv. Mater.* **2022**, *34*, No. 2104090.

(28) Zhao, C.; Wang, Y.; Li, Z.; Chen, W.; Xu, Q.; He, D.; Xi, D.; Zhang, Q.; Yuan, T.; Qu, Y.; et al. Solid-Diffusion Synthesis of Single-Atom Catalysts Directly from Bulk Metal for Efficient CO_2 Reduction. *Joule* **2019**, *3*, 584−594.

(29) Huang, M.; Wang, C.; Quan, L.; Nguyen, T. H.-Y.; Zhang, H.; Jiang, Y.; Byun, G.; Ruoff, R. S. CVD growth of porous graphene foam in film form. *Matter* **2020**, *3*, 487−497.

(30) Fan, Q.; Hou, P.; Choi, C.; Wu, T.; Hong, S.; Li, F.; Soo, Y.; Kang, P.; Jung, Y.; Sun, Z. Activation of Ni Particles into Single Ni-N Atoms for Efficient Electrochemical Reduction of CO_2. *Adv. Energy Mater.* **2020**, *10*, No. 1903068.

(31) Takele Menisa, L.; Cheng, P.; Qiu, X.; Zheng, Y.; Huang, X.; Gao, Y.; Tang, Z. Single atomic Fe-N_4 active sites and neighboring graphitic nitrogen for efficient and stable electrochemical CO_2 reduction. *Nanoscale Horiz.* **2022**, *7*, 916−923.

(32) Jiang, W.-J.; Gu, L.; Li, L.; Zhang, Y.; Zhang, X.; Zhang, L.; Wang, J.-Q.; Hu, J.-S.; Wei, Z.; Wan, L.-J. Understanding the High Activity of Fe-N-C Electrocatalysts in Oxygen Reduction: Fe/Fe_3C Nanoparticles Boost the Activity of Fe-Nx. *J. Am. Chem. Soc.* **2016**, *138*, 3570−3578.

(33) Zhang, H.; Hwang, S.; Wang, M.; Feng, Z.; Karakalos, S.; Luo, L.; Qiao, Z.; Xie, X.; Wang, C.; Su, D.; et al. Single Atomic Iron Catalysts for Oxygen Reduction in Acidic Media: Particle Size Control and Thermal Activation. *J. Am. Chem. Soc.* **2017**, *139*, 14143−14149.

(34) Rignanese, G. M.; Pasquarello, A.; Charlier, J. C.; Gonze, X.; Car, R. Nitrogen Incorporation at Si(001)−SiO2Interfaces: Relation between N1sCore-Level Shifts and Microscopic Structure. *Phys. Rev. Lett.* **1997**, *79*, 5174−5177.

(35) Wang, X.; Wang, Y.; Sang, X.; Zheng, W.; Zhang, S.; Shuai, L.; Yang, B.; Li, Z.; Chen, J.; Lei, L.; et al. Dynamic Activation of Adsorbed Intermediates via Axial Traction for the Promoted Electrochemical CO2 Reduction. *Angew. Chem., Int. Ed.* **2021**, *60*, 4192−4198.

(36) Zhao, C.; Dai, X.; Yao, T.; Chen, W.; Wang, X.; Wang, J.; Yang, J.; Wei, S.; Wu, Y.; Li, Y. Ionic Exchange of Metal-Organic Frameworks to Access Single Nickel Sites for Efficient Electroreduction of CO$_2$. *J. Am. Chem. Soc.* **2017**, *139*, 8078−8081.

(37) Chen, L. X.; Zhang, X.; Wasinger, E. C.; Attenkofer, K.; Jennings, G.; Muresan, A. Z.; Lindsey, J. S. Tracking Electrons and Atoms in a Photoexcited Metalloporphyrin by X-ray Transient Absorption Spectroscopy. *J. Am. Chem. Soc.* **2007**, *129*, 9616−9618.

(38) Shelby, M. L.; Lestrange, P. J.; Jackson, N. E.; Haldrup, K.; Mara, M. W.; Stickrath, A. B.; Zhu, D.; Lemke, H. T.; Chollet, M.; Hoffman, B. M.; et al. Ultrafast Excited State Relaxation of a Metalloporphyrin Revealed by Femtosecond X-ray Absorption Spectroscopy. *J. Am. Chem. Soc.* **2016**, *138*, 8752−8764.

(39) Hahn, J. E.; Co, M. S.; Spira, D. J.; Hodgson, K. O.; Solomon, E. I. Quantitative Cu(I) determination using X-ray absorption edge spectroscopy: Oxidation of the reduced binuclear copper site in type 2 depleted Rhus laccase. *Biochem. Biophys. Res. Commun.* **1983**, *112*, 737−745.

(40) Chmielewski, P. J.; Latos-Grażyński, L.; Olmstead, M. M.; Balch, A. L. Nickel Complexes of 21-Oxaporphyrin and 21, 23-Dioxaporphyrin. *Chem.—Eur. J.* **1997**, *3*, 268−278.

(41) Kim, H.; Shin, D.; Yang, W.; Won, D. H.; Oh, H.-S.; Chung, M. W.; Jeong, D.; Kim, S. H.; Chae, K. H.; Ryu, J. Y.; et al. Identification of Single-Atom Ni Site Active toward Electrochemical CO$_2$ Conversion to CO. *J. Am. Chem. Soc.* **2021**, *143*, 925−933.

(42) Ravel, B.; Newville, M. ATHENA, ARTEMIS, HEPHAESTUS: data analysis for X-ray absorption spectroscopy using IFEFFIT. *J. Synchrotron Radiat.* **2005**, *12*, 537−541.

(43) Li, Y.; Adli, N. M.; Shan, W.; Wang, M.; Zachman, M. J.; Hwang, S.; Tabassum, H.; Karakalos, S.; Feng, Z.; Wang, G.; et al. Atomically dispersed single Ni site catalysts for high-efficiency CO$_2$ electroreduction at industrial-level current densities. *Energy Environ. Sci.* **2022**, *15*, 2108−2119.

(44) Mohd Adli, N.; Shan, W.; Hwang, S.; Samarakoon, W.; Karakalos, S.; Li, Y.; Cullen, D. A.; Su, D.; Feng, Z.; Wang, G.; Wu, G. Engineering Atomically Dispersed FeN$_4$ Active Sites for CO$_2$ Electroreduction. *Angew. Chem., Int. Ed.* **2021**, *60*, 1022−1032.

(45) Zhao, X.; Yang, X.; Wang, M.; Hwang, S.; Karakalos, S.; Chen, M.; Qiao, Z.; Wang, L.; Liu, B.; Ma, Q.; et al. Single-Iron Site Catalysts with Self-Assembled Dual-size Architecture and Hierarchical Porosity for Proton-Exchange Membrane Fuel Cells. *Appl. Catal., B* **2020**, *279*, No. 119400.

(46) Ma, M.; Clark, E. L.; Therkildsen, K. T.; Dalsgaard, S.; Chorkendorff, I.; Seger, B. Insights into the carbon balance for CO$_2$ electroreduction on Cu using gas diffusion electrode reactor designs. *Energy Environ. Sci.* **2020**, *13*, 977−985.

(47) Wen, M.; Sun, N.; Jiao, L.; Zang, S.; Jiang, H. Microwave-Assisted Rapid Synthesis of MOF-Based Single-Atom Ni Catalyst for CO$_2$ Electroreduction at Ampere-Level Current. *Angew. Chem.* **2024**, *136*, No. e202318338.

(48) Zhang, X.; Wang, Y.; Gu, M.; Wang, M.; Zhang, Z.; Pan, W.; Jiang, Z.; Zheng, H.; Lucero, M.; Wang, H.; et al. Molecular engineering of dispersed nickel phthalocyanines on carbon nanotubes for selective CO$_2$ reduction. *Nat. Energy* **2020**, *5*, 684−692.

(49) Ren, W.; Tan, X.; Jia, C.; Krammer, A.; Sun, Q.; Qu, J.; Smith, S.; Schüler, A.; Hu, X.; Zhao, C. Electronic Regulation of Nickel Single Atoms by Confined Nickel Nanoparticles for Energy-Efficient CO$_2$ Electroreduction. *Angew. Chem., Int. Ed.* **2021**, *61* (26), No. e202203335.

(50) Chen, J.; Li, Z.; Wang, X.; Sang, X.; Zheng, S.; Liu, S.; Yang, B.; Zhang, Q.; Lei, L.; Dai, L. Promoting CO$_2$ electroreduction kinetics on atomically dispersed monovalent Zn^I sites by rationally engineering proton-feeding centers. *Angew. Chem., Int. Ed.* **2022**, *61*, No. e202111683.

(51) Fan, Z.; Luo, R.; Zhang, Y.; Zhang, B.; Zhai, P.; Zhang, Y.; Wang, C.; Gao, J.; Zhou, W.; Sun, L.; et al. Oxygen-Bridged Indium-Nickel Atomic Pair as Dual-Metal Active Sites Enabling Synergistic Electrocatalytic CO$_2$ Reduction. *Angew. Chem., Int. Ed.* **2023**, *62*, No. e202216326.

(52) Han, H.; Im, J.; Lee, M.; Choo, D. N-bridged Ni and Mn single-atom pair sites: A highly efficient electrocatalyst for CO$_2$ conversion to CO. *Appl. Catal., B* **2023**, *320*, No. 121953.

(53) Hao, J.; Zhu, H.; Zhuang, Z.; Zhao, Q.; Yu, R.; Hao, J.; Kang, Q.; Lu, S.; Wang, X.; Wu, J.; et al. Competitive Trapping of Single Atoms onto a Metal Carbide Surface. *ACS Nano* **2023**, *17*, 6955−6965.

(54) Li, S.; Zhao, S.; Lu, X.; Ceccato, M.; Hu, X. M.; Roldan, A.; Catalano, J.; Liu, M.; Skrydstrup, T.; Daasbjerg, K. Low-Valence Zn$^{\delta+}$ (0<δ<2) Single-Atom Material as Highly Efficient Electrocatalyst for CO2 Reduction. *Angew. Chem., Int. Ed.* **2021**, *60*, 22826−22832.

(55) Lin, L.; Li, H.; Yan, C.; Li, H.; Si, R.; Li, M.; Xiao, J.; Wang, G.; Bao, X. Synergistic Catalysis over Iron-Nitrogen Sites Anchored with Cobalt Phthalocyanine for Efficient CO$_2$ Electroreduction. *Adv. Mater.* **2019**, *31*, No. 1903470.

(56) Liu, W.; Bai, P.; Wei, S.; Yang, C.; Xu, L. Gadolinium Changes the Local Electron Densities of Nickel 3d Orbitals for Efficient Electrocatalytic CO$_2$ Reduction. *Angew. Chem., Int. Ed.* **2022**, *61*, No. e202201166.

(57) Su, J.; Zhang, J.; Chen, J.; Song, Y.; Huang, L.; Zhu, M.; Yakobson, B. I.; Tang, B.; Ye, R. Building a stable cationic molecule/electrode interface for highly efficient and durable CO$_2$ reduction at an industrially relevant current. *Energy Environ. Sci.* **2021**, *14*, 483−492.

(58) Verma, S.; Hamasaki, Y.; Kim, C.; Huang, W.; Lu, S.; Jhong, H.-R. M.; Gewirth, A. A.; Fujigaya, T.; Nakashima, N.; Kenis, P. J. A. Insights into the Low Overpotential Electroreduction of CO$_2$ to CO on a Supported Gold Catalyst in an Alkaline Flow Electrolyzer. *ACS Energy Lett.* **2018**, *3*, 193−198.

(59) Wang, C.; Hu, X.; Hu, X.; Liu, X.; Guan, Q.; Hao, R.; Liu, Y.; Li, W. Typical transition metal single-atom catalysts with a metal-pyridine N structure for efficient CO$_2$ electroreduction. *Appl. Catal., B* **2021**, *296*, No. 120331.

(60) Wang, C.; Liu, Y.; Ren, H.; Guan, Q.; Chou, S.; Li, W. Diminishing the Uncoordinated N Species in Co-N-C Catalysts toward Highly Efficient Electrochemical CO$_2$ Reduction. *ACS Catal.* **2022**, *12*, 2513−2521.

(61) Wang, Q.; Liu, K.; Fu, J.; Cai, C.; Li, H.; Long, Y.; Chen, S.; Liu, B.; Li, H.; Li, W.; et al. Atomically dispersed s-block magnesium sites for electroreduction of CO$_2$ to CO. *Angew. Chem., Int. Ed.* **2021**, *133*, 25445−25449.

(62) Wang, X.; Ding, S.; Yue, T.; Zhu, Y.; Fang, M.; Li, X.; Xiao, G.; Zhu, Y.; Dai, L. Universal domino reaction strategy for mass production of single-atom metal-nitrogen catalysts for boosting CO$_2$ electroreduction. *Nano Energy* **2021**, *82*, No. 105689.

(63) Wu, X.; Guo, Y.; Sun, Z.; Xie, F.; Guan, D.; Dai, J.; Yu, F.; Hu, Z.; Huang, Y.; Pao, C.; et al. Fast operando spectroscopy tracking in situ generation of rich defects in silver nanocrystals for highly selective electrochemical CO$_2$ reduction. *Nat. Commun.* **2021**, *12*, No. 660.

(64) Zhang, M.-D.; Huang, J.; Shi, W.; Liao, P.; Chen, X. Synergistic Effect in a Metal-Organic Framework Boosting the Electrochemical CO$_2$ Overall Splitting. *J. Am. Chem. Soc.* **2023**, *145*, 2439−2447.

(65) Zhang, X.; Li, W.; Chen, J.; Wu, X.; Liu, Y.; Mao, F.; Yuan, H.; Zhu, M.; Dai, S.; Wang, H.; et al. In Operando Identification of In Situ Formed Metalloid Zinc$^{\delta+}$ Active Sites for Highly Efficient Electrocatalyzed Carbon Dioxide Reduction. *Angew. Chem., Int. Ed.* **2022**, *61*, No. e202202298.

(66) Zhong, H.; Ghorbani-Asl, M.; Ly, K. H.; Zhang, J.; Ge, J.; Wang, M.; Liao, Z.; Makarov, D.; Zschech, E.; Brunner, E.; et al.

Synergistic electroreduction of carbon dioxide to carbon monoxide on bimetallic layered conjugated metal-organic frameworks. *Nat. Commun.* **2020**, *11*, No. 1409.

(67) Qiao, B.; Wang, A.; Yang, X.; Allard, L. F.; Jiang, Z.; Cui, Y.; Liu, J.; Li, J.; Zhang, T. Single-atom catalysis of CO oxidation using Pt_1/FeO_x. *Nat. Chem.* **2011**, *3*, 634−641.

(68) Kortlever, R.; Shen, J.; Schouten, K. J. P.; Calle Vallejo, F.; Koper, M. T. M. Catalysts and Reaction Pathways for the Electrochemical Reduction of Carbon Dioxide. *J. Phys. Chem. Lett.* **2015**, *6*, 4073−4082.

(69) Yang, X.; Cheng, J.; Xuan, X.; Liu, N.; Liu, J. Boosting Defective Carbon by Anchoring Well-Defined Atomically Dispersed $Ni-N_4$ Sites for Electrocatalytic CO_2 Reduction. *ACS Sustainable Chem. Eng.* **2020**, *8*, 10536−10543.

(70) Chen, X.; Liu, W.; Sun, Y.; Tan, T.; Du, C.; Li, Y. KOH-Enabled Axial-Oxygen Coordinated Ni Single-Atom Catalyst for Efficient Electrocatalytic CO_2 Reduction. *Small Methods* **2023**, *7*, No. 2201311.

(71) Kim, D.; Xie, C.; Becknell, N.; Yu, Y.; Karamad, M.; Chan, K.; Crumlin, E. J.; Nørskov, J. K.; Yang, P. Electrochemical Activation of CO_2 through Atomic Ordering Transformations of AuCu Nanoparticles. *J. Am. Chem. Soc.* **2017**, *139*, 8329−8336.

(72) Venna, S. R.; Jasinski, J. B.; Carreon, M. A. Structural evolution of zeolitic imidazolate framework-8. *J. Am. Chem. Soc.* **2010**, *132*, 18030−18033.

(73) Liu, X.; Ding, S.; Wei, Q.; Zhou, Y.; Zhang, P.; Xu, Z. DFT insights in to the hydrodenitrogenation behavior differences between indole and quinoline. *Fuel* **2021**, *285*, No. 119039.

(74) Wu, Q.; Dai, C.; Meng, F.; Jiao, Y.; Xu, Z. J. Potential and electric double-layer effect in electrocatalytic urea synthesis. *Nat. Commun.* **2024**, *15*, No. 1095.

(75) Schumann, J.; Stamatakis, M.; Michaelides, A.; Réocreux, R. Ten-electron count rule for the binding of adsorbates on single-atom alloy catalysts. *Nat. Chem.* **2024**, *16*, 749−754.

(76) Ngan, H. T.; Sautet, P. Tuning the Hydrogenation Selectivity of an Unsaturated Aldehyde via Single-Atom Alloy Catalysts. *J. Am. Chem. Soc.* **2024**, *146*, 2556−2567.

(77) Delley, B. From molecules to solids with the DMol[3] approach. *J. Chem. Phys.* **2000**, *113*, 7756−7764.

(78) Perdew, J. P.; Burke, K.; Ernzerhof, M. Generalized Gradient Approximation Made Simple. *Phys. Rev. Lett.* **1996**, *77*, 3865−3868.

(79) Pritom, R.; Jayan, R.; Islam, M. M. Unraveling the effect of single atom catalysts on the charging behavior of nonaqueous Mg-CO_2 batteries: a combined density functional theory and machine learning approach. *J. Mater. Chem. A* **2024**, *12*, 2335−2348.

(80) Kresse, G.; Joubert, D. From ultrasoft pseudopotentials to the projector augmented-wave method. *Phys. Rev. B* **1999**, *59*, 1758−1775.

(81) Momma, K.; Izumi, F. VESTA: a three-dimensional visualization system for electronic and structural analysis. *J. Appl. Crystallogr.* **2008**, *41*, 653−658.